

## GAS ACCRETION WITHIN THE DUST CAVITY IN AB AUR\*

PABLO RIVIÈRE-MARICHALAR,<sup>1</sup> ASUNCIÓN FUENTE,<sup>1</sup> CLÉMENT BARUTEAU,<sup>2</sup> ROBERTO NERI,<sup>3</sup>  
SANDRA P. TREVIÑO-MORALES,<sup>4</sup> ANDRÉS CARMONA,<sup>2</sup> MARCELINO AGÚNDEZ,<sup>5</sup> AND RAFAEL BACHILLER<sup>1</sup>

<sup>1</sup>*Observatorio Astronómico Nacional (OAN, IGN), Calle Alfonso XII 3 E-28014 Madrid, Spain*

<sup>2</sup>*CNRS / Institut de Recherche en Astrophysique et Planétologie, 14 avenue Edouard Belin, F-31400 Toulouse, France*

<sup>3</sup>*Institut de Radioastronomie Millimétrique, 300 rue de la Piscine, F-38406 Saint-Martin d'Hères, France*

<sup>4</sup>*Dept. of Space, Earth and Environment, Chalmers University of Technology, Onsala Space Observatory, SE-439 92 Onsala, Sweden*

<sup>5</sup>*Instituto de Física Fundamental, CSIC, Serrano 123, E-28006 Madrid, Spain*

(Received January 1, 2018; Revised January 7, 2018; Accepted June 28, 2019)

Submitted to ApJ Letters

### ABSTRACT

AB Aur is a Herbig Ae star hosting a well-known transitional disk. Because of its proximity and low inclination angle, it is an excellent object to study planet formation. Our goal is to investigate the chemistry and dynamics of the molecular gas component in the AB Aur disk, and its relation with the prominent horseshoe shape observed in continuum mm emission. We used the NOEMA interferometer to map with high angular resolution the  $J = 3-2$  lines of  $\text{HCO}^+$  and HCN. By combining both, we can gain insight into the AB Aur disk structure. Chemical segregation is observed in the AB Aur disk:  $\text{HCO}^+$  shows intense emission toward the star position, at least one bright molecular bridge within the dust cavity, and ring-like emission at larger radii, while HCN is only detected in an annular ring that is coincident with the dust ring and presents an intense peak close to the dust trap. We use  $\text{HCO}^+$  to investigate the gas dynamics inside the cavity. The observed bright  $\text{HCO}^+$  bridge connects the compact central source with the outer dusty ring. This bridge can be interpreted as an accretion flow from the outer ring to the inner disk/jet system proving gas accretion through the cavity.

*Keywords:* circumstellar matter — stars: pre-main sequence — protoplanetary disks — stars: individual (AB Auriga) — planet-disk interactions — planets and satellites: formation

Corresponding author: Pablo Rivière-Marichalar  
p.riviere@oan.es

\* Based on observations carried out with the IRAM Northern Extended Millimeter Array (NOEMA). IRAM is supported by INSU/CNRS (France), MPG (Germany), and IGN (Spain).

## 1. INTRODUCTION

AB Aur is a Herbig A0-A1 star (Hernández et al. 2004) located at  $162.9 \pm 1.5$  pc from the Sun (Gaia Collaboration 2018), which hosts a transitional disk. Near-IR observations with HST-STIS and SUBARU-CIAO showed that the disk presents spiral-arm signatures (Grady et al. 1999; Fukagawa et al. 2004; Hashimoto et al. 2011), which could be due to one or several giant-forming planets. Observations of CO J = 2-1,  $^{13}\text{CO}$  J = 2-1, and continuum at 1.3 mm with PdBI showed the presence of an inner dust cavity extending out to 70-100 au, surrounded by an asymmetric dusty ring (Piétu et al. 2005; Tang et al. 2012; Fuente et al. 2017). Higher spatial resolution sub-mm imaging resolved the inner disk (Tang et al. 2012). Furthermore, observations with the eVLA revealed the presence of a radio jet (Rodríguez et al. 2014), which is consistent with the high levels of accretion derived for the system (García López et al. 2006; Salyk et al. 2013). High angular resolution ( $0''.11 \times 0''.08$ ) ALMA images of the CO J = 2-1 line in AB Aur showed the existence of two prominent CO spiral arms at a radius of  $0''.3$  (Tang et al. 2017). Whether the spiral arms are connected with the outer dust ring remains to be clarified, as the aforementioned images were subject to strong filtering due to the limited  $uv$ -plane coverage, precluding the detection of large structures.

Our team is carrying out a long-term study of this prototypical disk. On the basis of the comparison of the continuum NOEMA maps at 2.2 and 1.1 mm with two-fluid (gas+dust) hydrodynamical simulations (Baruteau & Zhu 2016; Zhu & Baruteau 2016), Fuente et al. (2017) proposed the existence of a decaying vortex toward the mm dust emission peak, which is needed to explain, in the presence of azimuthal dust trapping, why the azimuthal contrast ratio along the (sub)mm ring is smaller at 2.2 mm than at 1.1 mm. The vortex is assumed to have formed at the outer edge of the gap carved by a massive planet, and its decay is caused by the disk turbulent viscosity. The study constrained the total mass of solid particles in the ring, which was found to be of the order of  $30 M_{\oplus}$ .

A handful of species were detected toward AB Aur using single-dish and interferometric observations (Fuente et al. 2010; Pacheco-Vázquez et al. 2015, 2016). Interferometric images of  $^{13}\text{CO}$  J = 2-1,  $\text{C}^{18}\text{O}$  J = 2-1, SO J = 5<sub>6</sub>-4<sub>5</sub>, and  $\text{H}_2\text{CO}$  J = 3<sub>0,3</sub>-2<sub>02</sub> with an angular resolution of  $\sim 1''.6 \times 1''.5$  testify to the complex gas chemistry occurring in the ring, which was found to be related with the gas dynamics. In particular, Pacheco-Vázquez et al. (2016) found a local minimum in the SO

abundance toward the dust trap, which was interpreted as the gas vortex chemical footprint.

In this Letter we extend our chemical and dynamical study to smaller spatial scales by using higher resolution images of the  $\text{HCO}^+$  J = 3-2 and HCN J = 3-2 lines, which provide new insights into the evolution of the gas in this protoplanetary disk.

## 2. OBSERVATIONS AND DATA REDUCTION

We present high spatial resolution  $\sim 0''.4$  ( $\sim 60$  AU at the distance of AB Aur) observations of the  $\text{HCO}^+$  J = 3-2 and HCN J = 3-2 lines in the AB Aur disk. The observations were carried out with the NOEMA interferometer in their A and C configurations. The observations in C configuration were carried out in 2017 January 1-3. During these observations, the wideband correlator WIDEX ( $\Delta\nu=2$  MHz) was used to cover the  $\sim 2$  GHz receiver band, and two correlator units providing a higher spectral resolution of  $\sim 39$  kHz were located at the frequencies of the  $\text{HCO}^+$  J = 3-2 and HCN J = 3-2 lines, respectively. The region empty of emission channels was used to build the 1.12 mm continuum published by Fuente et al. (2017). The observations in A configuration were done in 2018 March, using the new correlator PolyFix, which provides a total band of  $\sim 7.74$  GHz with a spectral resolution of  $\Delta\nu=2$  MHz. In addition, higher spectral resolution  $\Delta\nu=65$  kHz chunks were located at the frequencies of the  $\text{HCO}^+$  and HCN lines. All data from A and C configurations were resampled to a frequency resolution of 89 kHz and merged to build the A+C table of visibilities used to create the images shown in this Letter. In order to optimize the spatial resolution, we have applied uniform weighting to produce the  $\text{HCO}^+$  J = 3-2 image. In the case of the HCN J = 3-2 line, we prefer to use natural weighting because the weaker line emission. Self-calibration was applied to improve the sensitivity and dynamical range. Data calibration and imaging were done using the package GILDAS<sup>1</sup>/CLASS software.

## 3. RESULTS

As Figure 1 shows, the integrated intensity maps of the  $\text{HCO}^+$  J = 3-2 and HCN J = 3-2 lines unveil important differences in the distribution of the  $\text{HCO}^+$  and HCN emissions in the radial and azimuthal directions. While HCN is only detected (above  $5\sigma$ ) in an annular ring that is spatially coincident with the dust ring (hereafter, outer ring),  $\text{HCO}^+$  is detected in the outer ring and also features intense and compact emission to-

<sup>1</sup> See <http://www.iram.fr/IRAMFR/GILDAS> for more information about the GILDAS softwares.

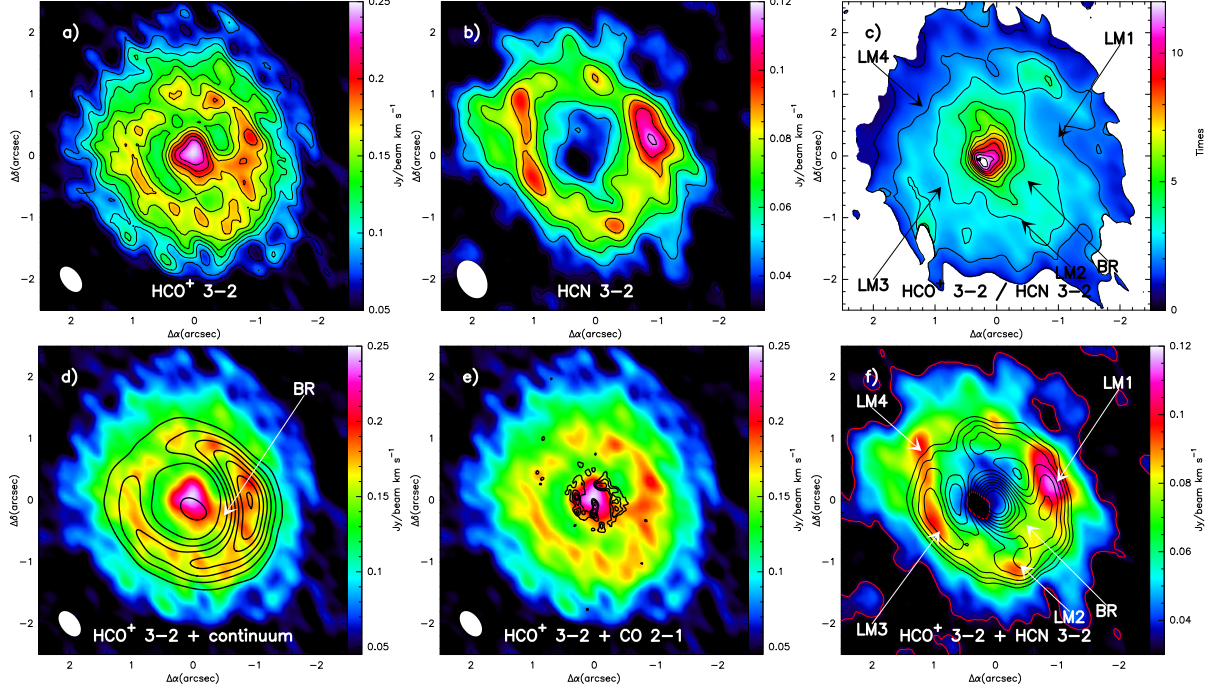


**Figure 1.** (a) Integrated intensity map of  $\text{HCO}^+$  using uniform weight. Contour levels are  $5\sigma$  to  $40\sigma$  in steps of  $4\sigma$ . (b) Integrated intensity map of HCN using natural weight. Contour levels are  $5\sigma$  to  $20\sigma$  in steps of  $1\sigma$ . (c) Map of  $\text{HCO}^+$  over HCN, using only channels with  $S/N > 5$ . Contour levels are 2 to 24 in steps of 4. (d) Integrated intensity map of  $\text{HCO}^+$  with continuum intensity map at 1.12 mm overlaid as white contours. Continuum contour levels are  $15\sigma$  to  $75\sigma$  in steps of  $10\sigma$ . (e) CO  $J = 3-2$  emission contours from Tang et al. (2017) overlaid on the  $\text{HCO}^+$   $J = 3-2$  image. (f) HCN integrated intensity map with  $\text{HCO}^+$  overlaid as black contours (natural weights).  $\text{HCO}^+$  contour levels are  $20\sigma$  to  $40\sigma$  in steps of  $1\sigma$ . The  $5\sigma$  level is also shown. Interesting positions in the maps are labeled in white. Integrated line intensity maps were built by integrating velocity channels between  $+2$  and  $+10 \text{ km s}^{-1}$ . Beam sizes are shown in the bottom-left corner of each plot.

ward the star position. Additionally, a bright  $\text{HCO}^+$  bridge connecting the compact central source with the outer ring (labeled BR in Figure 1) is observed. To test whether the bridge is due to an elongation of the central emission along the beam major axis, we show in Figure 2 a comparison of the spatially integrated line profiles of  $\text{HCO}^+$  at different positions. The line profile along the bridge (Figure 2(b)) is quite different from that of the central emission (Figure 2(a)): while the profile in the innermost region peaks at  $6.7 \text{ km s}^{-1}$  (close to the system velocity), with an FWHM of  $1.4 \text{ km s}^{-1}$ , the line profile at the bridge location is two-peaked, with a red-shifted wing at  $7.3 \text{ km s}^{-1}$  with an FWHM  $0.8 \text{ km s}^{-1}$  and a blueshifted broad and fainter wing at  $\sim 5.3 \text{ km s}^{-1}$ . The difference in the line profiles shows that the emission seen at the location of the bridge is not the elongation by the beam of the emission from the inner disk, thus a feature on its own.

In Figure 1e we compare our  $\text{HCO}^+$   $J = 3-2$  integrated intensity map with the CO  $J = 2-1$  observations by Tang et al. (2017). The southwestern spiral-arm observed in CO  $J = 2-1$  overlaps with the position of the  $\text{HCO}^+$   $J$

$= 3-2$  bridge in its southern side, indicating a possible connection between both structures.

We also find significant differences between the  $\text{HCO}^+$  and HCN emission maps along the azimuthal direction. In order to illustrate these differences we have labeled the HCN clumps along the outer ring as LM1 to LM4 (see Figure 1). The  $\text{HCO}^+$  emission in the outer ring follows quite well the dust emission with intensity variations  $< 2\sigma$  along it. This is in agreement with what we expect from two-fluid simulations (Fuente et al. 2017) in which the gas surface density is quite uniform along the ring, while large particles are still accumulated in the dust trap. We note that we measure an intensity contrast of a factor of  $\sim 3$  in the dust 1.12mm continuum emission. In contrast, the HCN emission seems to follow the spatial distribution of large particles, with the most intense clump, LM1, being spatially coincident with the dust trap. In the eastern-half disk where the 1.12mm continuum emission presents its minimum, the HCN emission seems to come from the external parts of the ring (see LM4 in Figure 1). Given the limited sensitivity of our maps it is important to note that LM2, LM3, and LM4 could be due to strong noise fluctuations.

Although the  $\text{HCO}^+$  and HCN are both high-density tracers, the two molecules present a different chemistry and are expected to come from different layers within the disk (Pacheco-Vázquez et al. 2015). HCN is known to be abundant in dense cold regions where CO and  $\text{HCO}^+$  are frozen on grains (Fuente et al. 2019). In addition, the emission of  $\text{HCO}^+$  might be optically thick toward the outer ring.

## 4. DISCUSSION

### 4.1. Gas inside the mm dust cavity

Low-resolution spectral observations of AB Aur are available from about  $1 \mu\text{m}$  up to about  $400 \mu\text{m}$  (Woitke et al. 2018). The detection of several O I, C II, C, OH, and ro-vibrational lines of CO and  $\text{H}_2$  prove the existence of warm gas (Brittain et al. 2003; Bitner et al. 2007; Riviere-Marichalar et al. 2016). The origin (inner disk, outflow, gas filling the cavity) of these line emissions is uncertain because of the moderate angular and spectral resolutions of the observations. Based on observations of the [O I]  $63 \mu\text{m}$  line, Riviere-Marichalar et al. (2016) concluded that part of the atomic oxygen emission is coming from the jet.

Interferometric (sub-)millimeter images provide insights into the gas and dust distributions. Out of all the molecular lines imaged with millimeter interferometers in AB Auriga (Piétu et al. 2005; Tang et al. 2012; Pacheco-Vázquez et al. 2016; Tang et al. 2017), only the high-resolution CO  $J = 2-1$  image reported by Tang et al. (2017) and our  $\text{HCO}^+$   $J = 3-2$  image show evidence of molecular emission within the cavity. These two lines present, however, different line profiles. Figure 2(a) shows integrated CO  $J = 2-1$  and  $\text{HCO}^+$   $J = 3-2$  spectra in the innermost region (see Figure 2(d)). The line profile of the  $\text{HCO}^+$  line shows a narrow,  $\Delta v = 1.4 \text{ km s}^{-1}$  component at  $6.7 \text{ km s}^{-1}$  on top of broad wings covering the  $\sim 0-10 \text{ km s}^{-1}$  velocity range. Although the CO  $J = 2-1$  line covers the same velocity range, its profile is flat-topped. As commented by Tang et al. (2017), the flat CO line profile can be due to self-absorption and spatial filtering effects. It should be noted that recent observations of CO  $J = 3-2$  and  $\text{HCO}^+$   $J = 3-2$  in AA Tau by Loomis et al. (2017) showed different spatial distribution of the  $\text{HCO}^+$   $J = 3-2$ , and CO  $J = 3-2$  emissions, suggesting that they are indeed coming from different regions.

The poor knowledge of the physical conditions of the gas within the cavity ( $r < 80 \text{ au}$ ) makes it difficult to derive molecular abundances. Woitke et al. (2018) calculated a gas mass of  $4.2 \times 10^{-4} M_{\odot}$  for the inner disk, with a column density of  $N_H \sim 3 \times 10^{22} \text{ cm}^{-2}$  at  $r \sim 40 \text{ au}$ . Assuming optically thin emission and that the

$\text{HCO}^+$   $J = 3-2$  line is thermalized at  $T_k = 150 \text{ K}$  (Tang et al. 2017), we derive  $N(\text{HCO}^+) = 3 \times 10^{13} \text{ cm}^{-2}$ , i.e., an  $\text{HCO}^+$  abundance of  $\sim 10^{-9}$  within the cavity, which is compatible with typical values in photo-dissociation regions (see, e.g., Fuente et al. 2003; Goicoechea et al. 2017; Ginard et al. 2012). The  $\text{HCO}^+$  abundance might be larger if the  $\text{HCO}^+$   $J = 3-2$  emission is optically thick.

### 4.2. $\text{HCO}^+/\text{HCN}$ : A chemical tool

Dramatic chemical segregation is found in the radial direction and along azimuth within the AB Aur disk. The absence of large grains within the cavity allows the UV irradiation from the star to penetrate through it and photo-dissociate molecules. Very few species are expected to survive in highly irradiated gas.  $\text{H}_2$  and CO are abundant enough to self-shield the stellar radiation (see, e.g., Sternberg & Dalgarno 1995). In addition, small hydrides (CH,  $\text{CH}^+$ , NH), reactive ions ( $\text{CO}^+$ ,  $\text{HOC}^+$ ), and simple oxygenated species such as OH and  $\text{HCO}^+$ , are detectable in the highly irradiated layers of photon-dominated regions (Fuente et al. 2003; Goicoechea et al. 2017). Because it is easily observable at millimeter wavelengths,  $\text{HCO}^+$  is an excellent candidate to investigate the gas dynamics within the cavities of nearby transition disks.

Our observations suggest that the  $\text{HCO}^+/\text{HCN}$  ratio is a useful chemical tool in determining the structure of transitional disks. In the case of unresolved disks, a high  $\text{HCO}^+/\text{HCN}$  intensity ratio might be associated with the existence of inner dust cavities full of dense gas. We note that, together with AB Aur, HD 142527 and AA Tau were the disks with a higher  $\text{HCO}^+$   $J = 3-2$  /  $\text{HCN}$   $J = 3-2$  ratio in the compilation of Pacheco-Vázquez et al. (2015). Both systems show filamentary gas emission through their dust cavities (Casassus et al. 2013; Loomis et al. 2017). The other disk with a high ratio, GM Aur, has not been studied in detail. This result is also in line with recent results by Alonso et al. (2018) toward the Herbig Be star R Mon.

### 4.3. Gas kinematics

We show in Figure 3a the first moment map of  $\text{HCO}^+$  emission. The outer parts of the disk resemble those of a Keplerian disk. However, twisted isophotes are observed toward the center ( $r < 0''.6$ ). The aforementioned twisting can be reproduced by two misaligned Keplerian disks as proposed by Hashimoto et al. (2011). A radial outflow would produce a similar effect (Rosenfeld et al. 2014). We adopt the misaligned disks as the most plausible explanation, as it is consistent with NIR observations by Hashimoto et al. (2011). In Figure 3b, we show the residual map that results from subtracting a two Keplerian disks model from the  $\text{HCO}^+$  first moment map.

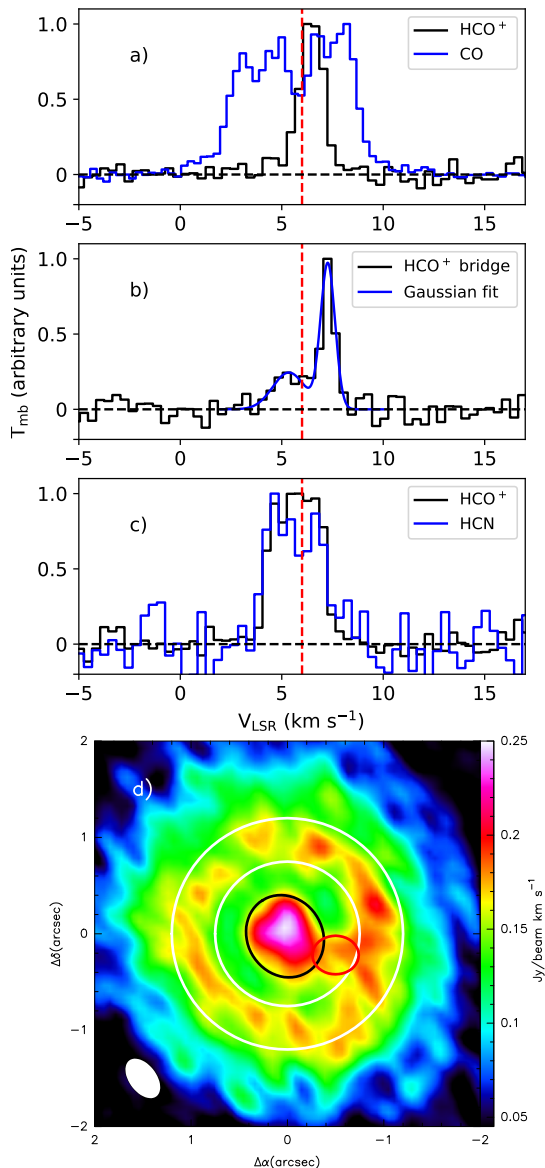


**Figure 2.** (a) Comparison of the spatially integrated line profile of CO  $J = 2-1$  (blue) from Tang et al. (2017) and  $\text{HCO}^+$   $J = 3-2$  (black) over the inner regions. The vertical dashed line displays the system velocity. (b) Spatially integrated  $\text{HCO}^+$  line profile over the bridge position. (c) Comparison of spatially integrated HCN and  $\text{HCO}^+$  line profiles over the outer ring. All the spectra have been scaled to their maximum values to allow for an easy comparison. (d) Location of the regions used to obtain the integrated spectra are shown as a black ellipse (innermost regions), a red ellipse (bridge), and white circles (ring).

The model consists of an outer disk extending from 350 to 45 au, with  $i = 26^\circ$  and  $\text{PA} = 37^\circ$ , and an inner one extending from 45 au inward with  $i = 43^\circ$  and  $\text{PA} =$

$65^\circ$  (Hashimoto et al. 2011), around a  $2.4 M_\odot$  star, and the final image is convolved with the observational beam. This simplistic model provides a reasonable fit across the disk, except in the southwestern region, where strong residuals are observed. Visual inspection of Figure 3a, shows that there is an anomaly (blue circle) in the velocity field that is spatially coincident with the bridge (BR, Figure 3b). This anomaly is due to high-velocity wings in the line profile of  $\text{HCO}^+$  at the bridge position (see Figure 2b). The red-shifted peak is compatible with Keplerian rotation, while the blue-shifted one requires a different mechanism, most likely infalling gas. To test the possibility that the blue shifted wing is tracing infalling material, we built a pure free-falling velocity field following equation

$$v_{\text{free-fall}} = \sqrt{2GM_* \times \left( \frac{1}{r} - \frac{1}{r_{\text{start}}} \right)} \quad (1)$$

where  $r_{\text{start}}$  is the starting position for free-fall accretion, and we adopted  $r_{\text{start}} = 120$  au (accretion starts at the inner edge of the dust ring,  $r \sim 0''.7$ ). We assumed that infall stops at 40 au. Cuts in the first-moment map, and in our convolved models are shown in Figure 3c. The free-falling model has a velocity of  $5.5 \text{ km s}^{-1}$  at the bridge position, compared to the  $5.3 \text{ km s}^{-1}$  derived from the Gaussian fit. Therefore, some of the material in the bridge seems to be infalling at a velocity close to free-fall. Smaller velocities, such as the speed of sound, which is typically 0.05-0.1 times the Keplerian velocity, cannot account for the blue-shifted component. Assuming that this component is due to accretion, we derive a mass accretion  $3 \times 10^{-8}$  to  $3 \times 10^{-7} M_\odot \text{ yr}^{-1}$  (for  $X(\text{HCO}^+) = 10^{-9}$  to  $10^{-8}$ ), comparable to a value of  $1.2 \times 10^{-7} M_\odot \text{ yr}^{-1}$  by Salyk et al. (2013).

Radial inflows through dust cavities have been invoked before to explain different features observed in a few protoplanetary disks, such as gas and dust streamers and twisted isophotes (Casassus et al. 2013; Dutrey et al. 2014; Perez et al. 2015; Zhang et al. 2015; Loomis et al. 2017; Mendigutia et al. 2017; Walsh et al. 2017). In particular, Zhang et al. (2015) proposed radial inflows to explain absorption features observed in CO ro-vibrational lines in AA Tau, with material moving at velocities close to free-fall in regions between the inner and outer disk. The presence of gap-crossing radial inflows could explain the high accretion levels derived for some transitional disks, such as those observed in AB Aur (Garcia Lopez et al. 2006; Salyk et al. 2013). A compact and collimated bipolar jet was detected by Rodríguez et al. (2014) in the continuum at 7 mm suggesting the existence of a disk-jet system. In order to sustain it, gas must flow through the cavity and

reach the inner regions of the system, otherwise accretion would drain the inner disk on very short timescales.

We cannot discard the possibility that the non-Keplerian component observed along the bridge is due to gas out of the disk plane, in which case, depending on the exact location of the bridge, it might be interpreted as an inflow or an outflowing stream.

Previous work by this team proposed that the asymmetric dust ring is caused by dust trapping in a decaying gas vortex formed at the outer edge of the gap carved by a massive planet, coincident with the position of the bridge (Fuente et al. 2017). Higher-spatial resolution observations, with facilities such as ALMA, are needed to understand the connection between the HCO+ bridge in the cavity and the putative planet responsible for the outer dust ring.

## 5. SUMMARY AND CONCLUSIONS

We used the NOEMA interferometer to map with high angular resolution the HCO+ and HCN  $J = 3-2$  lines. Based on these interferometric data, we explored the chemistry and dynamics of the molecular gas component in the AB Aur disk, and its relationship with the decaying gas vortex found in it. We detected ring-like emission in HCN, spatially coincident with dust emission. HCO+ shows a ring-like structure in the outer re-

gions, plus a compact source at the center. We suggest that the HCO+/HCN ratio is a useful tool to discern the presence of dense gas in dust cavities.

Our most prominent result is the detection of a filamentary HCO+ emission structure that connects the outer disk with the inner regions. A simple model consisting of two misaligned Keplerian disks with an infall component along the bridge can reproduce our observations, suggesting the presence of active accretion within the dust cavity. Yet, alternative explanations involving gas out of the disk plane cannot be ruled out. The possible connection of the observed bridge with a planet formation scenario requires further research.

We thank the anonymous referee for a fruitful report that helped us to improve the discussion of our results. We thank the Spanish MINECO for funding support from AYA2016-75066-C2-1/2-P, AYA2012-32032 and ERC under ERC-2013-SyG, G. A. 610256 NANOCOSMOS. This work was supported by the Programme National “Physique et Chimie du Milieu Interstellaire” (PCMI) of CNRS/INSU with INC/INP co-funded by CEA and CNES. S.P.T.M. acknowledges to the European Union’s Horizon 2020 research and innovation program for funding support given under grant agreement No.639459 (PROMISE).

## REFERENCES

- Alonso-Albi, T., Riviere-Marichalar, P., Fuente, A., et al. 2018, *A&A*, 617, A31
- Baruteau, C. & Zhu, Z. 2016, *MNRAS*, 458, 3927
- Bitner, M. A., Robinson, E. L., & Behr, B. B. 2007, *ApJ*, 662, 564
- Brittain, S. D., Rettig, T. W., Simon, T., et al. 2003, *ApJ*, 588, 535
- Casassus, S., van der Plas, G., M, S. P., et al. 2013, *Nature*, 493, 191
- Casassus, S., Marino, S., Pérez, S., et al. 2015, *ApJ*, 811, 92
- Dutrey, A., di Folco, E., Guilloteau, S., et al. 2014, *Nature*, 514, 600
- Fuente, A., Baruteau, C., Neri, R., et al. 2017, *ApJL*, 846, L3
- Fuente, A., Cernicharo, J., Agúndez, M., et al. 2010, *A&A*, 524, A19
- Fuente, A., Navarro, D., Caselli, P., et al. 2018, *A&A*, 624, A105
- Fuente, A., Rodríguez-Franco, A., García-Burillo, S., Martín-Pintado, J., & Black, J. H. 2003, *A&A*, 406, 899
- Fukagawa, M., Hayashi, M., Tamura, M., et al. 2004, *ApJL*, 605, L53
- Gaia Collaboration, 2018, *VizieR Online Data Catalog*, I/345
- García Lopez, R., Natta, A., Testi, L., & Habart, E. 2006, *A&A*, 459, 837
- Ginard, D., González-García, M., Fuente, A., et al. 2012, *A&A*, 543, A27
- Goicoechea, J. R., Cuadrado, S., Pety, J., et al. 2017, *A&A*, 601, L9
- Grady, C. A., Woodgate, B., Bruhweiler, F. C., et al. 1999, *ApJ*, 523, L151
- Hashimoto, J., Tamura, M., Muto, T., et al. 2011, *ApJ*, 729, L17
- Hernández, J., Calvet, N., Briceño, C., Hartmann, L., & Berlind, P. 2004, *AJ*, 127, 1682
- Loomis, R. A., Öberg, K. I., Andrews, S. M., MacGregor, M. A. 2017, *ApJ*, 840, 23
- Mendigutía, I., Oudmaijer, R. D., Garufi, A., et al. 2017, *A&A*, 608, A104
- Pacheco-Vázquez, S., Fuente, A., Agúndez, M., et al. 2015, *A&A*, 578, A81
- Pacheco-Vázquez, S., Fuente, A., Baruteau, C., et al. 2016, *A&A*, 589, A60

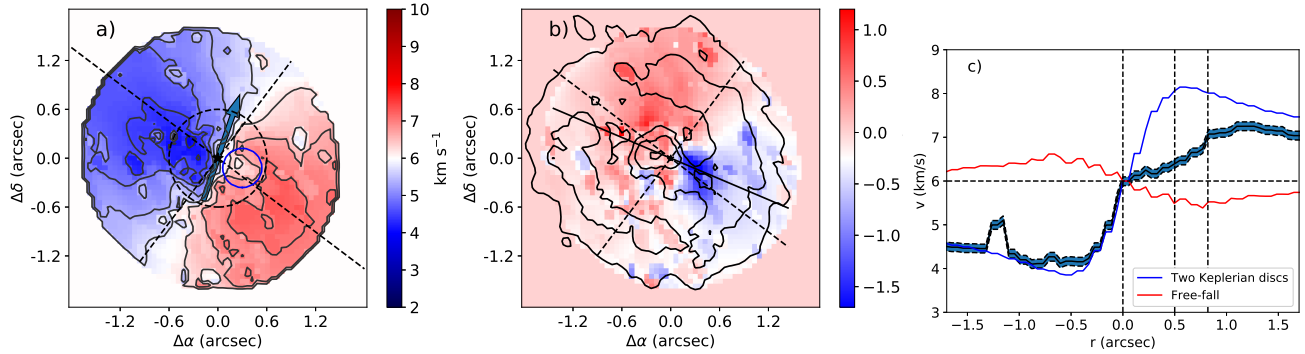


**Figure 3.** (a)  $\text{HCO}^+$  first moment map. The two dashed lines show the direction of the disk major and minor axes. The arrow marks the position of the radio jet (Rodríguez et al. 2014). The blue circle marks the position of a velocity anomaly associated with the bridge. (b) Residuals of a model consisting of two Keplerian disks (see Section 4.3). Solid contours depict  $5\sigma$  to  $25\sigma$  levels of the integrated line intensity. The black solid line shows the direction of the cut through the bridge used for panel (c). (c) Cut along the velocity anomaly for the  $\text{HCO}^+$  first moment map (black lines with dashed region), a two Keplerian disks model as in panel (b) (blue line), and a free-falling component (red line). The dashed vertical lines mark the positions of the center, the bridge, and the inner edge of the dust disk.

Perez, S., Casassus, S., Ménard, F., et al. 2015, *ApJ*, 798, 85  
 Piétu, V., Guilloteau, S., & Dutrey, A. 2005, *A&A*, 443, 945  
 Riviere-Marichalar, P., Merín, B., Kamp, I., Eiroa, C., & Montesinos, B. 2016, *A&A*, 594, A59  
 Rodríguez, L. F., Zapata, L. A., Dzib, S. A., et al. 2014, *ApJ*, 793, L21  
 Rosenfeld, K. A., Chiang, E., Andrews, S. M. 2014, *ApJ*, 782, 62  
 Salyk, C., Herczeg, G. J., Brown, J. M., et al. 2013, *ApJ*, 769, 21

Sternberg, A. & Dalgarno, A. 1995, *ApJS*, 99, 565  
 Tang, Y.-W., Guilloteau, S., Dutrey, A., et al. 2017, *ApJ*, 840, 32  
 Tang, Y.-W., Guilloteau, S., Piétu, V., et al. 2012, *A&A*, 547, A84  
 Walsh, C., Daley, C., Facchini, S., Juhász, A. 2017, *A&A*, 697, A114  
 Woitke, P., Kamp, I., Antonellini, S., et al. 2018, arXiv e-prints  
 Zhang, K., Crockett, N., Salyk, C., et al. 2015 *ApJ*, 805, 55  
 Zhu, Z. & Baruteau, C. 2016, *MNRAS*, 458, 3918